Jupiter's Atmospheric Temperatures: From Voyager IRIS to Cassini CIRS

Amy A Simon-Miller

NASA/Goddard Space Flight Center, Code 693.0, Greenbelt, MD 20771

Barney J. Conrath, Peter J. Gierasch

Cornell University, Space Sciences Bldg., Ithaca, NY 14853

Glenn S. Orton

Jet Propulsion Laboratory, Pasadena, CA

Richard K. Achterberg

SSAI/ Goddard Space Flight Center, Code 693.0, Greenbelt, MD 20771

F. Michael Flasar

NASA/Goddard Space Flight Center, Code 693.0, Greenbelt, MD 20771

Brendan Fisher

Jet Propulsion Laboratory, Pasadena, CA

Submitted: February 20, 2004

Figures: 12

Manuscript: 44 pages

Keywords: Jupiter, atmosphere; Atmospheres, dynamics; Atmospheres, temperature

Proposed Running Head: Jupiter's Atmospheric Temperatures

Corresponding Author Information:

Amy Simon-Miller

NASA GSFC

Code 693.0

Greenbelt, MD 20771

301-286-6738

Amy.Simon@nasa.gov

Abstract

Retrievals run on Cassini Composite Infrared Spectrometer data obtained during the distant Jupiter flyby have been used to generate global temperature maps of the planet in the troposphere and stratosphere. Similar retrievals were performed on Voyager 1 IRIS data and have provided the first detailed IRIS map of the stratosphere. In both data sets, high latitude troposphere temperatures are presented for the first time, and the meridional gradients indicate the presence of circumpolar jets. Thermal winds were calculated for each data set and show strong vertical shears in the zonal winds at low latitudes.

The temperatures retrieved from the two spacecraft were also compared with yearly ground-based data obtained over the intervening two decades. Tropospheric temperatures reveal gradual changes at low latitudes, with little obvious seasonal or short-term variation (Orton *et al.* 1994). Stratospheric temperatures show much more complicated behavior over short timescales, consistent with quasi-quadrennial oscillations at low latitudes, as suggested in prior analyses of shorter intervals of ground-based data (Orton *et al.* 1991, Friedson 1999). A scaling analysis indicates that meridional motions, mechanically forced by wave or eddy convergence, play an important role in modulating the temperatures and winds in the upper troposphere and stratosphere on seasonal and shorter time scales. At latitudes away from the equator, the mechanical forcing can be derived simply from a temporal record of temperature and its vertical derivative. Ground-based observations with improved vertical resolution and/or long-term monitoring from spacecraft are required for this purpose.

Introduction

The twin Voyager spacecraft and the Cassini mission flew by Jupiter over 20 years apart (March 1979, July 1979 and late December 2000 closest approaches). This time separation spans over a Jovian year and a half. Comparison of the data sets received from these missions should reveal seasonal differences and long-term changes. In particular, mid- and far-infrared data allow mapping of the planet's atmospheric temperatures at a variety of heights by using radiances at wavelengths where gaseous methane and molecular hydrogen provide the dominant opacity (Conrath and Gautier 1980).

While there is value in a direct comparison of the spacecraft data sets that were acquired during different Jovian seasons, the temporal sampling is quite limited. However, there are extensive ground-based data, primarily from the NASA Infrared Telescope Facility (IRTF), over the period between the Voyager and Cassini observations. The vertical resolution of this data is much poorer than that of the spacecraft observations, particularly in the stratosphere. Nevertheless, these data have shown interesting interannual and seasonal variability (Orton *et al.* 1991, 1994, Friedson 1999), and their temporal coverage forms a valuable complement to the spacecraft observations. Thus, we use the ground-based data to interpolate between the two epochs to interpret the spacecraft data more fully.

In Section 1, we summarize the two instruments used to obtain infrared spectra on Voyager and Cassini and then discuss the data sets that were selected for analysis. Section 2 explains the analysis techniques used on the data to calculate temperature fields and gradient winds. Section 3 compares the two data sets in the context of the ground-based data, seasonal effects and non-seasonal variability. It also discusses the implications of the observed temperature record for meridional circulations. We conclude with a summary of recommended future work.

1. Instruments and Data Sets

1.1 The Fourier Transform Spectrometers

The Infrared Interferometer Spectrometers (IRIS) onboard Voyager 1 and 2 both obtained spectra of Jupiter in 1979 during their grand tours of the outer solar system. Both spacecraft passed within 750,000 km of Jupiter and IRIS achieved spatial resolutions up to 250 km at closest approach. Data were obtained throughout the flyby, and spectra with nearly global coverage were obtained during north-south mapping sequences performed about three million km from Jupiter. The IRIS instrument was a dual interferometer-radiometer with a shared 0.25° (4.36 milliradian) circular field of view (Hanel *et al.* 1977, 1980a, 1980b). The single-channel radiometer was sensitive from .33–2 microns (Hanel *et al.* 1980a), while the Michelson interferometer was sensitive to radiation from 200 to 2500 cm^{-1} (~4-50 microns) with an apodized spectral resolution of 4.3 cm^{-1}. The Voyager 1 and 2 IRIS interferometers did not have equal responsivities, with Voyager 1 being

superior to Voyager 2, due to a slight misalignment of the Voyager 2 IRIS beamsplitter (Hanel *et al.* 1980a). For this reason, Voyager 1 data will mainly be considered in this paper.

In late 2000, Cassini began a distant swingby of Jupiter (~10 million km closest approach) en route to Saturn. Used as an opportunity to shake down the spacecraft and instrument operations, observations were obtained from approximately October 2000 through March 2001. The Composite Infrared Spectrometer (CIRS) on Cassini is comprised of three separate focal planes, covering the spectral range of 10 to 1400 cm^{-1} (1 mm to 7 μm) with an adjustable (apodized) spectral resolution from 0.5 to 15 cm^{-1}. The mid-infrared Michelson interferometer has two focal plane arrays, FP3 and FP4, sensitive from 600 to 1125 cm^{-1} (~11-16 microns) and 1100 to 1450 cm^{-1} (~7-11 microns), respectively. Both are 1x10 pixel cooled HgCdTe arrays (one is photovoltaic, the other photoconductive) with 0.27-mrad spatial resolution. The far-infrared polarizing interferometer, in focal plane FP1, is sensitive to radiation between 10 and 650 cm^{-1} (15–1000 microns) and has two thermopile detectors with a single 3.9-mrad circular field of view. More detailed discussions of the CIRS instrument and investigation are given by Kunde *et al.* (1996) and Flasar *et al.* (2004b). At Jupiter CIRS acquired spectra with maximum spatial resolution of about 2.4° of latitude for FP3 and FP4, but only hemispheric coverage for FP1.

1.2 Data Sets

Voyager data exist from many days before and after each Jupiter flyby. North-south mapping sequences obtained spectra with global coverage at a range of about 3 million km. In these sequences, the IRIS field of view stepped repeatedly from north to south across Jupiter's disk along the subspacecraft meridian, with intervening flybacks. As the spacecraft approached the planet, higher spatial resolution coverage was obtained. For this analysis, data were selected based on several criteria, first requiring that the range to the planet be less than 4 million km. The Voyager 1 data are of better quality, as discussed above, and only those spectra were used for latitudes equatorward of +/- 60° planetographic latitude. Data were also chosen to have an emission angle less than 60 degrees. The spectra were then hand-edited to remove any noisy spectra. To fill in high latitude coverage, both Voyager 1 and 2 data were selected. These spectra fell in the range of +/- 60°-75° planetographic latitude and were constrained to have emission angles less than 78°, to maintain the validity of the plane-parallel approximation used in the temperature retrievals. Any spectra whose FOV projections were partially off the planet were also removed.

The Cassini–era temperature maps were constructed from 'beach-ball' maps, so-named because they were designed to interleave CIRS north-south scans with Cassini imaging science mosaics. The scans were offset so that two rotations of the planet would provide global coverage. Though this technique means that atmospheric changes (from motions of thermal features) could occur in between the two rotations and affect the maps, such effects would be much smaller than the CIRS spatial resolution. Four maps of this type

were obtained, separated by a total of 10 days. To retrieve the most spatial information, we use the map acquired on January 1, 2001, nearest to closest approach, for analysis.

The ground-based observations reported here, acquired at the NASA/IRTF Facility, include those up to 1995 discussed by Orton *et al.* (1991, 1994), Friedson *et al.* (1995), and Friedson (1999), but they also extend to 2000 for comparison with CIRS. Stratospheric temperatures were retrieved from IRTF observations of emission from the ν_4 band of CH_4 at 7.6 μm (1306 cm^{-1}). Before 1994, the observations were taken with a single-element detector using a discrete 0.8-μm wide filter centered at 7.9 μm which was scanned along Jupiter's central meridian as Jupiter rotated underneath it or along a rectangular grid to create a 2-dimensional image, as described in some detail by Orton *et al.* (1991). From 1994 onward, observations of Jupiter's stratospheric CH_4 emission were made using middle-infrared cameras with a 1.8% circular variable filter centered on the P-branch of the ν_4 band at 7.85 μm. Determination of the actual absorption from this band is complicated by the presence of absorption from the same band in the Earth's atmosphere. The relative motion of Earth and Jupiter causes a Doppler shift between the lines in the two atmospheres and requires a careful correction to obtain the actual Jovian emission. The corrected radiance, normalized for nadir viewing, is sensitive to an atmospheric layer centered at 10-20 mbar pressure.

Tropospheric temperatures retrieved from IRTF observations were obtained with a discrete filter, 0.5 μm wide and centered at 18.7 μm (535 cm^{-1}), where collision-induced H_2 absorption dominates the atmospheric opacity. Just as for the stratospheric

observations, single-element scanning was replaced by 2-dimensional imaging in 1994 and thereafter. For both the tropospheric and stratospheric observations, absolute radiances were obtained by assuming that the disk average radiance is constant in time, and using Voyager IRIS as a standard.

2. Analysis Techniques

2.1 IRIS and CIRS Temperature Retrievals

The temperature retrieval algorithm used with the IRIS and CIRS data is described in detail in Conrath *et al.* (1998). A constrained inversion is applied to the spectral radiances, yielding low-pass filtered temperature profiles that are consistent with the information content of the measurements. Tropospheric temperatures were obtained from measurements within the broad, collision-induced S(0) and S(1) hydrogen absorption lines centered at 354 cm^{-1} and 600 cm^{-1}, respectively. The required absorption coefficients were calculated using the codes of Borysow (Borysow *et al.* 1985, Birnbaum *et al.* 1996) and include H_2-H_2 and H_2-He interactions. A hydrogen mole fraction of 0.86 was used, based on the Galileo probe results (von Zahn *et al.* 1998, Niemann *et al.* 1996). Stratospheric temperatures were obtained from measurements within the CH_4 ν_4 band centered near 1300 cm^{-1}. For rapid calculation of atmospheric opacities in this part of the spectrum, the correlated-k formulation was used. A height-independent CH_4 mole fraction of 1.8×10^{-3}, the Galileo probe value, was assumed (Niemann *et al.* 1996). Figure

1 shows selected inversion kernels from both spectral regions, illustrating the portions of the troposphere and stratosphere from which information can be obtained.

Fig 1. Contribution Functions

For tropospheric temperature retrievals from individual Voyager IRIS spectra, the spectral intervals 320-430 cm^{-1} and 520-600 cm^{-1} were used. The portions of the Jupiter spectrum below 320 cm^{-1} and between 320 and 430 cm^{-1} were excluded because of the possible presence of cloud opacity. Wavenumbers greater than ~600 cm^{-1} were not used because of the rapidly decreasing signal-to-noise ratio in this region of the individual IRIS spectra. Since the portions of the Jupiter spectrum used are sensitive to the molecular hydrogen ortho-para ratio, it was necessary to simultaneously infer the vertical profile of the para hydrogen fraction along with the temperature profile. Because of the relatively low signal-to-noise ratio of the individual IRIS measurements in the 1300 cm^{-1} region, it was necessary to construct averaged spectra within latitude bins 10° in width prior to performing the stratospheric temperature inversions. In order to obtain sufficient numbers of spectra in each average, the Voyager stratospheric temperature analysis was confined to the latitude range 60° S to 60° N. Strong filtering was required in the retrievals, resulting in very limited vertical structure information. Nevertheless, it is possible to infer the gross stratospheric thermal structure at the time of the Voyager encounter.

Because of the relatively low spatial resolution obtained with CIRS FP1 during the Cassini flyby, it was not possible to use the same 320-600 cm^{-1} spectral region that was used in the IRIS retrievals. Instead, FP3 measurements between 600 and 690 cm^{-1} were used. The presence of absorption by gases with spatially varying abundances prevents the inclusion of measurements at wavenumbers greater than ~690 cm^{-1}. Since it is not possible to uniquely obtain both the para hydrogen fraction and the temperature profile from this spectral region alone, only the temperature profile was retrieved under the assumption of equilibrium para hydrogen. Because of the relatively weak sensitivity in this part of the spectrum to the para hydrogen fraction, this assumption should not introduce significant errors into the retrieved temperatures. Stratospheric temperatures were obtained from the CIRS spectra using measurements in the same 1300 cm^{-1} CH_4 absorption region that was used in the IRIS retrievals. Because of the substantially lower Noise Equivalent Spectral Radiance (NESR) in the CIRS FP4 measurements relative to the IRIS measurements (and to a lesser extent the higher spectral resolution), significantly more information on stratospheric thermal structure can be obtained from the CIRS spectra. The CIRS retrievals from the combined FP3 and FP4 data provide information between approximately 1 and 20 mbar in the stratosphere and 150 and 400 mbar in the troposphere.

Zonal mean meridional temperature cross sections for latitudes smaller than 55° were constructed from the individual retrievals from both IRIS and CIRS and are shown in Fig. 2. Both sets of retrieved temperatures shown are latitudinally smoothed versions of the maps, with 5° binning and smoothing on a latitude grid with 2.5° separation. Also

included in the figure for comparison is the more limited thermal stratospheric structure inferred from the 10° latitude-bin averaged IRIS spectra. In both the CIRS and IRIS data, the stratosphere and troposphere retrievals are combined with a linear interpolation between 20 and 100 mbar. High-latitude tropospheric temperature cross sections are shown in Fig. 3.

Fig 2. Global Temperature maps

Fig 3. Polar troposphere retrievals

2.2 Thermal Winds

The meridional temperature variations seen in Fig. 2 can be used to calculate the zonal winds. Assuming geostrophic and hydrostatic balance, the latitudinal temperature variations are related to the vertical shears in the zonal winds by the thermal wind equation (Andrews *et al.* 1987, Salby 1996):

$$u_T = -\frac{R}{f}\left(\frac{\partial T}{\partial y}\right)_p \ln\left(\frac{p_0}{p_1}\right) \qquad (1)$$

where u_T is the zonal wind increment (or thermal wind) over each pressure interval, R is the gas constant and equals 3.745×10^3 J K^{-1} kg^{-1} for Jupiter, f is the latitude-dependent Coriolis parameter, ∂T is the temperature difference (in K) over the latitude interval ∂y

(in meters) and p_0 and p_1 are the pressures at the bottom and top of the vertical sampling bins. The temperature retrievals performed on the IRIS and CIRS data were spaced such that $ln(p_0/p_1)$ was a constant for each map, though the spacing did vary slightly between the IRIS stratosphere and troposphere retrievals.

The thermal winds are very sensitive to noise in the temperature plots, and the smoothed temperature meridional cross sections in Fig. 2 have been used to generate cross sections of wind velocity with height, as shown in Fig. 4. At the bottom pressure of the retrievals, the velocities were assumed to be those of the cloud-tracked winds obtained by the Voyager and Cassini imaging science instruments (*e.g.*, Simon 1999, Porco *et al.* 2003). The thermal winds cannot be derived near the equator, because f goes to zero in (1), and errors in the retrieved temperatures magnify without limit. Therefore, latitudes within 5° of the equator have been avoided.

Fig. 4 – Thermal winds

2.3. Temperatures Retrieved from IRTF Observations

Figure 5 shows plots of temperature vs. latitude for the upper troposphere at 250 mbar (left) and the stratosphere at 10-20 mbar (right), for 1980 through 2000 (Orton *et al.* 1991, 1994, Friedson 1999). Each year's profile is offset by roughly 5 K for clarity. Because of telluric absorption and the limited spectral resolution used, the information on stratospheric temperatures corresponds to the average temperature in a thick slab centered

at 10-20 mbar (Orton *et al.* 1991, Friedson 1999). The stratospheric temperatures shown here represent those at 20 mbar. They have been taken from a linear vertical profile, constrained to have a fixed temperature at the 100-mbar level, whose gradient was varied to match the corrected radiances in the CH_4 ν_4 band, described earlier. This is similar to the procedure used by Orton *et al.* (1991). Tropospheric temperatures were derived from the observed radiances at 18.7 μm by perturbing a baseline temperature profile uniformly until the upwelling radiance at the given emission angle matched the observation. The baseline profile was taken as a smoothed average of the Voyager-1 radio occultation profiles. This is the same approach used by Orton *et al.* (1994).

Fig 5. Latitudinal Scans at 250 and 20 mbar

3. Discussion

3.1 High Latitudes

The high-latitude tropospheric temperature maps generated in Fig. 3 from the CIRS and IRIS data all show evidence of temperature gradients, and therefore, a high latitude wind jet near 100 mbar. High latitude winds have been seen near the cloud deck (see Porco *et al.* (2003), for example) and are expected to extend higher into atmosphere. While the evidence of a wind jet found from the temperature maps is much higher in altitude (100 mbar vs. ~700 mbar) and seems to non-continuous with the cloud top gradients, it still may be an extension of the cloud top winds. Although IRIS stratosphere retrievals were

not possible at these high latitudes, CIRS retrievals show evidence of winds at even higher altitude, up to ~1 mbar. Studies of ultraviolet Hubble Space Telescope data have also found indications of motion in the polar stratosphere (Vincent *et al.* 2000). The polar vortices implied by these results can have significant dynamical and compositional ramifications, as they do in Earth's polar atmosphere. It should be noted that the strength and presence of a polar vortex can be modified by many factors (Baldwin *et al.* 2001), including the solar cycle, planetary waves and even equatorial forcing, similar to those we discuss in the next section. A more detailed analysis of both ground-based and CIRS high latitude data is currently in progress and will be reported elsewhere.

3.2 Temporal Behavior at Low and Mid Latitudes

The temperatures and zonal winds in Figs. 2 and 4 retrieved from CIRS spectra are similar to those reported by Flasar *et al.* (2004a). Paramount in the zonal wind cross section is the intense equatorial stratospheric jet centered near the 4-mbar level. Flasar *et al.* (2004a) have suggested this is associated the ~4-year oscillation in the zonally averaged stratospheric temperatures that has been seen in ground-based observations and thought to be driven by propagating waves (Orton *et al.* 1991, Leovy *et al.* 1991). The temperatures and derived zonal-winds observed by Voyager IRIS provide an important comparison with those obtained from Cassini CIRS. To facilitate the comparison, Figure 6 illustrates the zonal mean temperatures of Fig. 2 relative to a global mean vertical temperature profile determined separately for the IRIS and CIRS data.

Fig. 6

Fig. 7 compares the zonal thermal winds (eq. 1) at 250 and 20 mbar calculated from CIRS (solid line) and IRIS (dotted line) data. To better highlight the differences, the cloud-top winds have not been included. These new IRIS tropospheric results compare well with those obtained by Gierasch *et al.* (1986). Though the troposphere winds are similar poleward of 20° latitude, noticeable differences are evident at low latitudes, near 15°-20° latitude and the equator.

Major differences are found in the equatorial upper troposphere between 20° N and 20° S. The temperatures observed by CIRS are more nearly symmetric about the equator and show that the equator is ~4 K colder than adjacent latitudes, whereas there is little evidence of this cold trough in the temperatures retrieved from IRIS data. The low-latitude temperature variation dominates the time record of the 250-mbar temperatures derived from ground-based observations (Fig. 5). Almost immediately after the 1979 Voyager observations, the equatorial region cooled and reached a minimum temperature around 1984. Thereafter the equatorial temperatures maintained a local minimum in latitude. They rose again until 1990–1991, and subsequently decreased. Fig. 5 indicates that the cold trough has been noticeably deepening since 1995. At mid and high latitudes, the tropospheric temperatures from CIRS and IRIS are similar.

Fig 7: Thermals winds vs latitude (CIRS and IRIS) at 250 mbar and 20 mbar

The IRTF observations (Fig. 5) indicate that the stratospheric temperatures are more variable than those in the troposphere. This is also evident in the difference temperature cross sections for IRIS and CIRS (Fig. 6). Much of the stratospheric structure is associated with a ~4 year oscillation in equatorial temperatures (Orton *et al.* 1991, Friedson 1999). Leovy *et al.* (1991) have suggested that this temporal behavior in the zonal-mean temperatures (and zonal winds) is driven by the stresses associated with vertically propagating waves, analogous to the quasi-biennial (~26 month) oscillation (QBO) in the terrestrial stratosphere (Baldwin *et al.* 2001). The high vertical resolution afforded by the CIRS (and IRIS) temperature and zonal wind retrievals is consistent with this hypothesis, as noted earlier. Modeling of the so-called quasi-quadrennial oscillation (QQO) on Jupiter indicates that the stratospheric response to the wave forcing extends down to the tropopause region (Friedson 1999, Li and Read 2000), which is also supported by the data discussed here. Figure 7 indicates that the zonal winds are most affected at low latitudes in both the troposphere and stratosphere, and this may reflect a QQO response.

To examine the temporal behavior of the low-latitude thermal structure in Fig. 5 more closely, Figure 8 displays the difference of the equatorial temperature with the average of 15° N and S temperatures for the troposphere (250 mbar, left) and stratosphere (20 mbar, right). A cyclical 4-year variation, with arbitrary, fixed amplitude, is plotted for reference. The time series shown in Fig. 5 for both the stratosphere and troposphere suggest the possible superposition of thermal responses with several different periods. However, the stratospheric data in Fig. 8 suggest the presence of a QQO component.

Periodicities in the troposphere are less evident. The main seen is the large negative excursion in the temperature difference after 1996, related to the deepening of the equatorial cold trough discussed above. While there may be a lag between the stratospheric and tropospheric differences, a cross-correlation of the two data sets yields little of significance.

Fig 8 – Potential QQO variation

Figure 9 displays the Lomb-Scargle periodograms (Press *et al.* 1992) for the temperature differences shown in Fig. 8. Long-period variations or trends were not of interest, so a quadratic least squares fit was removed from the data (instead of the mean value or a linear fit) before performing the analysis. The resultant signals, show no significant periodicity (confidence levels <50%) in the troposphere, consistent with the preceding discussion. The stratospheric periodogram exhibits a pair of peaks with periodicities at 3.5 and 4.3 years, but these are also not very significant. This is perhaps not so surprising as the QQO (and the terrestrial QBO) is the nonlinear dynamical response of the atmosphere to forcing by wave stresses, and it is not a simple periodic phenomenon.

Fig 9 – QQO periodogram analysis

The stratospheric temperatures retrieved from both IRIS and CIRS also show a hemispheric asymmetry, with the northern hemisphere being warmer. The Voyager IRIS data were obtained just before northern autumnal equinox, while the Cassini CIRS data

were acquired closer to northern summer solstice, over 20 years (1.75 jovian years) later. In addition to smaller-scale variations, the overall hemispheric contrast also varies markedly with time.

Fig 10.

Can the hemispheric contrast seen in Figs. 2, 5, and 6 be a response to solar forcing? Jupiter has two components of seasonal modulation in its insolation: 1) an axial tilt of ~3° and 2) an orbital eccentricity of 0.048, with perihelion occurring ~0.1 jovian year prior to northern summer solstice (Beebe *et al.* 1986). To examine possible seasonal forcing, the temperature differences between northern and southern hemisphere latitudes as a function of time shown in Fig. 10 were checked for periodic variation using a Lomb-Scargle periodogram analysis (Press *et al.*, 1992). Because of calibration differences between data sets, only relative temperature differences could be examined, rather than individual latitude variations, and residual systematic offsets were removed with a linear least-squares fit to the differenced data. Figure 11 shows the resulting periodograms for the troposphere (250 mbar, top) and the stratosphere (10-20 mbar averages, bottom), with confidence levels labeled to show significance. The only meaningful periods occur at mid to high latitudes in the stratosphere where a signal with a period of roughly a Jovian year is evident. Correlation analyses can further elucidate whether the variation in the hemispheric contrast can simply be a radiative response to the modulation of solar forcing. Figure 12 displays the cross correlation between the hemispheric contrast (T(40N) – T(40S)) and the subsolar latitude. The stratospheric temperature contrast is

largest ~1 year after the northern summer solstice, *i.e.*, the contrast lags the solar forcing by ~1 year, whereas the tropospheric temperature contrast lags the solar forcing by a greater amount, ~2.5 years. The simplest model of radiative response is a linear relaxation to a radiative equilibrium temperature (see eq. (A6) in the Appendix). The relaxation is characterized by the radiative time constant, τ_r, and it is often expressed in combination with the orbital frequency, Ω_s. Conrath *et al.* (1990) explicitly calculated the relaxation of thermal perturbations in the upper tropospheres and stratospheres of the outer planets. For Jupiter they obtained $\Omega_s\tau_r$ ~4–5 at 10–20 mbar and ~ 2 at 250 mbar, respectively. In the simple linear model, the lag is $tan^{-1}(\Omega_s\tau_r)$; for an orbital period of 11.86 years, this amounts to 2.5–2.6 years at 10-20 mbar and 2.1 years at 250 mbar. The computed lag in the stratosphere does not agree with that given by the cross correlation. Moreover, the model indicates the greater lag should be in the stratosphere, contrary to what the cross correlations indicate. Finally, the hemispheric temperatures differences in Fig. 10 indicate that southern hemisphere summer troposphere is generally warmer than that of the north, which is not expected from the phasing of Jupiter's northern hemisphere summer and its perihelion and any reasonable lagged radiative model (Orton *et al.* 1994). Thus, seasonal variations in Jupiter's atmosphere do not appear to be simply radiatively controlled.

Fig 11. Seasonal variations – periodogram

Fig 12. Cross-correlation

3.2. Mechanical Forcing and Meridional Circulations

Several lines of evidence suggest that dynamical transport may play a critical role in modulating temperatures in Jupiter's upper troposphere and stratosphere: The variation on seasonal time scales does not seem consistent with a radiative response to solar forcing. Previous studies have suggested that the low-latitude spatial structure and temporal variation are consistent with wave forcing analogous to the terrestrial QBO (Leovy 1991, Friedson 1999, Li and Read 2000). This also pertains to the progressively colder zonal mean temperatures in the upper troposphere at the equator since 1994. While this coincides with the aftermath of the Comet Shoemaker-Levy (SL9) impacts at 45° S, which generated an increase in aerosol opacity that descended to the lower stratosphere and spread equatorward over the next several years (Friedson *et al.* 1999), it is hard to attribute this simply to a radiative response to the enhanced stratospheric haze. The meridional profiles of temperature at low latitudes are roughly symmetric about the equator, whereas the perturbed haze distribution is definitely not.

Appendix A considers the response of a zonally averaged (residual) meridional circulation driven by relaxation to radiative equilibrium and mechanical forcing. The source of the latter is not known a priori, but it includes momentum convergence of propagating disturbances that are unsteady or non-conservative: radiatively damped or dissipative, unstable, or otherwise transient. This class includes the waves thought to force the terrestrial QBO, and they drive meridional circulations that affect the stratospheric circulation and thermal structure globally (Baldwin *et al.* 2001). The stratosphere above the 20-mbar level is particularly simple, as the radiative time constant

is large enough that radiative effects can be neglected to first order on seasonal and shorter time scales. In this case the adiabatic heating and cooling associated with vertical motions dominate. Temperatures increasing (decreasing) with time indicate local subsidence (upwelling). The hemispheric temperature contrast in the stratosphere provides a useful example. From Fig. 5, mid-latitude temperature differences vary ~6 K over 3 years. From eq. (A3′), this implies vertical velocities ~0.002 cm s^{-1} in each hemisphere. Lower latitude temperature variations seem to be a maximum of ~8 K over 2 years, requiring vertical velocities on the order of 0.005 cm s^{-1}. A priori, these vertical velocities seem reasonable, and they are comparable to previous estimates for upward velocities within the Great Red Spot near the tropopause (~0.0045 cm s^{-1}, Conrath *et al.* 1981) and vertical motions associated with belts and zones (0.004 and 0.008 cm s^{-1} Gierasch *et al.* 1986, Conrath *et al.* 1990, West *et al.* 1992). Localized moist convective cells, with smaller lateral scales, have even higher velocities (Gierasch *et al.* 2000).

Vertical and meridional motions are related by continuity, so the observed variation in the temperature field implies both the vertical and meridional velocities. The mechanical forcing G follows, because it balances the Coriolis acceleration due to the meridional velocity. The quantity G can be directly related to the observed temperature field fairly simply (eq. A5′′). If radiative effects are important (as they are in the upper troposphere), a radiative equilibrium model is also required to solve for G. Eq. (A5′′) indicates that determining the mechanical forcing requires adequate resolution of both the vertical structure of temperature and of its temporal behavior. The existing spacecraft and ground-based observations present a bit of a quandary here. Both CIRS and IRIS

spectra have provided temperature maps with good vertical resolution (Fig. 2). However, they provide little in the way of temporal coverage: two snapshots nearly two jovian years apart. The ground-based observations provide a reasonably good temporal record of temperature behavior. However, they only provide two altitudes, one in the troposphere, one in the middle stratosphere.

4. Conclusions and Future Work

Jupiter's atmosphere is a dynamically active environment. Considerable effort has been directed toward quantifying the winds at the cloud-top level and processes such as small-scale convection (*e.g.*, Smith *et al.* 1979a, b, Porco *et al.* 2003, Gierasch *et al.* 2000). Yet, as discussed here, thermal-infrared observations both from spacecraft and ground-based telescopes are demonstrating that the upper troposphere and stratosphere, at altitudes above the clouds, are as rich in dynamical activity as they are on Earth. Propagating waves seem to play a key role in modulating the temperatures and circulation of these regions on Jupiter.

We have shown that a temporal record of Jupiter's temperature field in its stratosphere and upper troposphere provides a probe of its residual meridional circulation in these regions. Moreover, it allows one to derive the wave/eddy convergence that drives this circulation. The difficulty is that one requires a temporal record of both temperature and its vertical gradient with good spatial resolution, and current spacecraft and ground-based data sets do not provide this. Enhancements in ground-based capabilities may improve

the situation. Spectrometers (*e.g.*, TEXES: Lacy *et al.* 2002, Greathouse *et al.* 2003) with spectral resolution ~0.02 cm^{-1} in the ν_4 band of CH_4 currently exist. Although the terrestrial atmosphere still blots out incoming emission from the Q-branch, P-branch lines can be observed, offering the possibility of high vertical resolution over a good portion of the middle and upper stratosphere. A long-term spacecraft orbiting Jupiter is another possibility. Atmospheric temperatures could be mapped with good vertical resolution by successive radio occultations at different latitudes, or alternatively, by a thermal infrared sounder with reasonable spectral resolution (3-10 cm^{-1}) and limb-viewing capabilities.

It is important to develop a time-dependent radiative seasonal model of Jupiter's atmosphere. Radiative forcing is expected to contribute to the dynamics of circulations in the upper troposphere. The mid-latitude stratosphere exhibits a strong annual signature (Fig. 11), but with a lag relative to the radiative forcing that is significantly shorter than that predicted on the basis of estimated relaxation times (Fig. 12). In fact direct radiative effects should be secondary there, because the relaxation times are long. However, there may be an indirect radiative effect on the stratosphere. Radiative forcing may modify the tropopause region where the time constants are shorter, and subtly affect the vertical propagation of disturbances from the troposphere into the stratosphere. All this, of course, is speculative and needs to be better quantified.

More information on meridional circulations can be gotten from existing data. One approach to discriminating between cyclic or aperiodic variability is to decrease the coarseness of the time grid of the ground-based observations. While only one observing

epoch was sampled per year in Fig. 5, several successful observing runs per year at the IRTF took place between 1995 and 2002 to support several Galileo spacecraft encounters with Jupiter. These data have not yet been fully reduced and transformed into temperature maps, but once that is accomplished, a much stronger statistical basis will be available to distinguish medium- and short-term variability. In addition, the data set consists of observations taken through several medium-band filters, which should enable temperature retrieval between 100 and 400 mbar pressure, allowing variability as a function of depth to be explored more fully. Unfortunately, a similar data set does not exist for the stratosphere.

The residual mean meridional circulation, inferred from the time record of temperatures and their vertical gradients, is in many cases similar to the Lagrangian circulation, which describes the motion of quasi-conserved tracers (see Appendix A). In the troposphere, secondary tracers include constituents whose spatial distribution is a function of vertical motions. The most obvious of these is cloud distribution, and a careful comparison of both the horizontal and vertical distribution of clouds between the Voyager, Galileo and Cassini time frames is of value. NH_3 gas, *i.e.*, the mixing ratio above the condensation level, is also a tracer of vertical motions (Conrath and Gierasch 1986, Gierasch *et al.* 1986). The distribution of PH_3 gas acts as a tracer, since it is a disequilibrium constituent whose mixing ratio above the radiative-convective boundary is a strong function of vertical mixing. The distribution of both NH_3 and PH_3 are available from the Voyager era and have now been measured in the Cassini era (Gierasch *et al.* 1986, Achterberg *et al.* 2003, Irwin *et al.* 2003). Both show significant latitudinal and longitudinal variations

(Achterberg *et al.* 2003, Irwin *et al.* 2003) Much of the earth-based data in 1995-2002 included observations of radiances that are sensitive independently to the optical thickness of NH_3 ice cloud opacity, as well as uncondensed NH_3 gas. Ground-based observations, in particular those obtained around the 1994 impacts of Comet Shoemaker-Levy 9 into Jupiter, also have sensitivity to the phosphine mixing ratio. Galileo data acquired from 1995 to 2001 can also be used to measure these abundances (see Baines *et al.* 2002, for example). Reduction and analysis of these data sets will also provide the means to monitor vertical mixing between the spacecraft epochs.

The para fraction of H_2 is also an important dynamical tracer. Para fractions retrieved from Voyager IRIS spectra were found to be in disequilibrium: the para fractions in the upper troposphere at low latitudes were found to be closer to the equilibrium values at deeper warmer atmospheric levels, where the temperatures exceed 300 K (Conrath and Gierasch 1994, Conrath *et al.* 1998). This suggests low-latitude upwelling over time scales short compared to the para-fraction equilibration time (~10^9 s). Local regions like the Great Red Spot also stand out as low para fraction anomalies relative to their surroundings, presumably because of strong internal convection and vertical motions (Simon-Miller *et al.* 2002). The best spatial resolution of Cassini CIRS in the far infrared (~0.5 jovian radius) was insufficient to map the para fraction on Jupiter., but most ground-based middle-infrared data contain maps of Jupiter at 18 and 24 microns, two radiances which can be used to determine the para-H_2 mixing ratio as a function of position for a single atmospheric level.

Finally, atmospheric waves themselves can be characterized by existing thermal-infrared data. The CIRS temperature maps reported by Flasar *et al.* (2004a) indicated several trains of thermal features spaced along latitude bands. Several in the stratosphere exhibited westward movement. A detailed spectral analysis of these features can provide important clues to their propagation characteristics and aid in their identification as waves (Achterberg and Flasar 1996). This can lead to estimates of momentum fluxes.

Appendix A: Stratospheric Circulation

Following Andrews *et al.* (1987), the quasi-geostrophic equations for zonally averaged flows for thermal wind balance (A1), continuity (A2), heat balance (A3) and angular momentum (A4) are:

$$f_0 \frac{\partial u}{\partial z} + \frac{R}{H}\frac{\partial T}{\partial y} = 0, \tag{A1}$$

$$\frac{\partial v}{\partial y} + \frac{1}{\rho_0}\frac{\partial}{\partial z}(\rho_0 w) = 0, \tag{A2}$$

$$\frac{\partial T}{\partial t} + \frac{N^2 H}{R} w = \frac{T_e - T}{\tau_r}, \tag{A3}$$

$$\frac{\partial u}{\partial t} - f_0 v = G, \tag{A4}$$

where u, v and w are the zonally-averaged velocities in the x (eastward), y (northward) and z (vertical) directions, R is the gas constant (~3745 J K^{-1} kg^{-1} for Jupiter), H is a pressure scale height, N is the Brunt-Väisälä, frequency, τ_r is the radiative relaxation time, f_0 is the Coriolis frequency at a fixed latitude, $\rho_0(z)$ is the zonally averaged vertical mass density profile, T is the departure of the temperature from the zonal-averaged temperature, and T_e corresponds to the instantaneous equilibrium temperature, a measure of the thermal forcing in the system. The velocities v and w are the transformed-Eulerian mean residual velocities (see, *e.g.*, Andrews *et al.* 1987). In addition to Eulerian transport they include the transport of heat and momentum by eddies and waves. G is the mechanical forcing of the system, by any means, but likely due to eddy and/or wave convergence. For disturbances that are steady and conservative, *i.e.*, adiabatic, frictionless, not externally forced, G=0. Dunkerton (1978) has shown that under these conditions the transformed-Eulerian residual velocities in the earth's stratosphere and mesosphere correspond to the Lagrangian circulation, which describes constituent transport. Disturbances internally forced by an instability or radiatively or frictionally damped can lead to G≠0.

These equations may be combined to yield:

$$\frac{\partial^2}{\partial y^2}\frac{\partial T}{\partial t}+\frac{\partial}{\partial z}\left[\frac{1}{\rho_0}\frac{\partial}{\partial z}\left(\rho_0\frac{f_0^2}{N^2}\frac{\partial T}{\partial t}\right)\right]-\frac{\partial}{\partial z}\left[\frac{1}{\rho_0}\frac{\partial}{\partial z}\left(\rho_0\frac{f_0^2}{N^2}\frac{T_e-T}{\tau_r}\right)\right]+\frac{Hf_0}{R}\frac{\partial^2 G}{\partial y\partial z}=0. \quad \text{(A5)}$$

Using scaling arguments, the relative importance of each term can be determined. Consider first the radiative relaxation on seasonal timescales, where the balance is between the first and third terms of eq. (A3):

$$\frac{\partial T^{(r)}}{\partial t} = \frac{T_e - T^{(r)}}{\tau_r}, \tag{A6}$$

where $T^{(r)}$ denotes the radiative solution. Denoting the temporal amplitude of the seasonal variation by δT ($\delta T^{(r)}$), writing $\partial_t \sim \Omega_s$, where $2\pi/\Omega_s$ is Jupiter's orbital period, 11.9 years, and rearranging terms:

$$\frac{\left|T_e - T^{(r)}\right|}{\delta T^{(r)}} \sim \Omega_s \tau_r. \tag{A6'}$$

From Conrath *et al.* (1990), $\Omega_s \tau_r \sim$ 4-5>>1 for the upper and middle stratosphere (1–20 mbar), implying $|T_e - T^{(r)}| >> |\delta T^{(r)}|$. The available data do not support this. From Fig. 5, δT is comparable in magnitude to the hemispheric temperature differences. It is reasonable to assume that the latter are comparable to $|T_e - T^{(r)}|$. The time-marching radiative calculations by Besanger *et al.* (1986) are in agreement with this assumption, at least away from the polar regions. Thus, a radiative response to solar heating should not provide a good solution to variations in the upper and middle stratosphere on seasonal timescales. The tropopause region (~100 mbar) is somewhat different. Here $\Omega_s \tau_r \sim 2$ (Conrath *et al.*, 1990), and radiative effects should be more important. Even in this situation, however, we expect meridional motions to play a key role in Jupiter's

atmospheric response, as discussed next. Note that radiative effects become more important on longer time scales, even in the stratosphere. Formally, this corresponds to decreasing Ω_s from the seasonal value.

Consider next the large-scale hemispheric contrasts observed in the data (Figs. 2, 5, 6). It makes sense to examine cross-equatorial circulations with a scale comparable to Jupiter's planetary radius. The ratio of the first and second terms in eq. (A5) provides a horizontal scaling for the circulation, defined by the Burger number, B:

$$B = \frac{N^2 H^2}{f_0^2 L^2}.$$

For the mid-latitude stratosphere and tropopause, $N \sim 0.02$ s^{-1}, $H \sim 23$ km and $f \sim 2\text{x}10^{-4}$ s^{-1}. Taking $L \sim 71000$ km, it follows that $B \sim 0.001 << 1$, and the first term of equation (A5) can be ignored. For seasonal (or shorter) time scales in the stratosphere, $\Omega_s \tau_r >> 1$, and the third term is also negligible Integrating over z, we are left with:

$$\frac{1}{\rho_0}\frac{\partial}{\partial z}\left(\rho_0 \frac{f_0^2}{N^2}\frac{\partial T}{\partial t}\right) + \frac{H f_0}{R}\frac{\partial G}{\partial y} = 0. \qquad \text{(A5′)}$$

The heat and angular momentum and equations reduce to:

$$\frac{\partial T}{\partial t} + \frac{N^2 H}{R} w = 0, \qquad \text{(A3′)}$$

$$f_0 v = G. \qquad \text{(A4')}$$

The heat equation indicates that temperature variations are associated with vertical motions and the associated adiabatic heating and cooling. The vertical velocity, w, can be found by looking at the temperature variations themselves. The angular momentum equation (A4′) states that Coriolis torques balance the mechanical forcing. From continuity, the meridional velocities can be determined from the vertical motion field, hence the mechanical forcing can be determined from the temperature field and its temporal variation. Eq. (A5′) states this more directly, and shows that G can be directly inferred from a temporal record of T. However, terms with $\partial T/\partial z$ are involved, so temperatures must be mapped with good vertical resolution.

In the lower stratosphere and tropopause region, radiative relaxation is more important, and the full heat equation (A3) is relevant. Eq. (A5) then reduces to:

$$\frac{1}{\rho_0}\frac{\partial}{\partial z}\left(\rho_0 \frac{f_0^2}{N^2}\frac{\partial T}{\partial t}\right) - \frac{1}{\rho_0}\frac{\partial}{\partial z}\left(\rho_0 \frac{f_0^2}{N^2}\frac{T_e - T}{\tau_r}\right) + \frac{H f_0}{R}\frac{\partial G}{\partial y} = 0. \qquad \text{(A5'')}$$

Hence G can still be directly obtained from a time series of the temperature field, but now a radiative-equilibrium solution is also needed.

For lower latitude behavior associated with a QQO-type signal, the horizontal scale is smaller, but even with L ~17500 km (14° latitude), it is still large enough that $B << 1$, provided one is sufficiently far away from the equator. To estimate this, write $f = \beta y$, and set $L = y$. Then with N and H as given above, and $\beta = 5\times10^{-9}$ s^{-1} km^{-1} near the equator, $B = 1$ implies $y = 9600$ km, or 8° latitude from the equator. This defines the "tropical response" region, where the acceleration term ($\partial u/\partial t$) in eq. (A4) becomes important (Baldwin *et al.* 2001). In this case G must be obtained by replacing f_0 by βy, and then integrating (A5) in both y and z.

A simplified version of Eq. (A5) can be used to place previous stratospheric structure studies in context. To do this, it is helpful to write a scaled, dimensionless version. Let temperature variations, both temporal and spatial, be scaled by δT. Scale variations of T_e by the same quantity. Scale G by writing

$$G = M\frac{\delta u}{\tau_r}\hat{G}, \tag{A7}$$

where $\hat{G}$ is dimensionless and assumed to be of order unity. M is a dimensionless amplitude coefficient. Use the thermal wind relation (A1) to evaluate δu in terms of δT. Let $y = L\hat{y}$, where $\hat{y}$ is dimensionless, and make similar definitions for other variables. Assume that N, H and τ_r are constants. Eq. (A5) becomes

$$\frac{\partial^2}{\partial\hat{y}^2}\frac{\partial\hat{T}}{\partial\hat{t}} + \frac{\partial}{\partial\hat{z}}\left[\frac{1}{\hat{\rho}_0}\frac{\partial}{\partial\hat{z}}\left(\hat{\rho}_0\frac{f_0^2L^2}{N^2H^2}\frac{\partial\hat{T}}{\partial\hat{t}}\right)\right] - \frac{\partial}{\partial\hat{z}}\left[\frac{1}{\hat{\rho}_0}\frac{\partial}{\partial\hat{z}}\left(\hat{\rho}_0\frac{f_0^2L^2}{N^2H^2}\frac{\hat{T}_e-\hat{T}}{\Omega_s\tau_r}\right)\right] + \frac{M}{\Omega_s\tau_r}\frac{\partial^2\hat{G}}{\partial\hat{y}\partial\hat{z}} = 0 \tag{A5'''}$$

There have been two detailed studies of stratospheric dynamics on Jupiter, by Conrath *et al.* (1990) and by West *et al.* (1992). Three comments are important.

1. Conrath *et al.* (1990) solved numerically for both global-scale radiative forcing and for jet-scale lower boundary forcing. For the jet-scale forcing, the objective was to study the vertical decay of the mean zonal winds in the upper troposphere and stratosphere, and there was no time dependence in the forcing. In this application, $f_0^2 L^2/(N^2 H^2) \sim 1$. The balance is therefore between the last two terms on the left hand side of (A5‴). Good agreement with data was obtained for $M = 1$, with a form for $\hat{G}$ based on a Rayleigh friction (linear drag) assumption. Dimensionally, this gives G of order $\delta u/\tau_r$. Thus at least within the upper troposphere and lower stratosphere, and away from the equator, a viable hypothesis is that G is dominated by drag, probably wave drag.
2. For global-scale radiative forcing, Conrath *et al.* (1990) retained the same linear drag, and found stratospheric temperatures that varied seasonally by amplitudes that we now know are too small. As discussed above, this probably indicates that G contains a wave forcing component in the stratosphere, and that this component is larger than the wave drag component that dominates in the upper troposphere. In terms of (A5‴), this means that

$$M \sim \frac{f_0^2 L^2}{N^2 H^2} \Omega_s \tau_r, \tag{A8}$$

which indeed is larger than unity.

3. West *et al.* (1992) improved on the radiative heating treatment by including aerosol absorption of sunlight, neglected by Conrath *et al* (1990). West *et al* (1992). found that this heating is large, and led to disagreement between observed temperatures and predicted ones. They concluded that a strong wave forcing is needed, at least within the stratosphere. They pointed out that the structure of the dynamical forcing can be deduced if temperature observations exist and if radiative heating can be accurately evaluated. Their conclusion is consistent with (A8). Thus West *et al* (1992). also concluded that dynamical forcing is important, as we do here, but they reached the conclusion for different reasons. Here we stress the discrepancy between observed temperatures and the radiative solution. West *et al.* based their arguments on radiative heating calculations. At that time, there were not yet detailed temperature observations.

References

Achterberg, R. K., and F. M. Flasar 1996. Planetary-scale thermal waves in Saturn's upper troposphere. *Icarus* **119**, 350-369.

Achterberg, R. *et al.* 2003. Cassini CIRS measurements of temperature and ammonia abundance in Jupiter's upper troposphere: implications for dynamics. *Icarus,* in prep.

Andrews, D., J. Holton and C. Leovy 1987. *Middle Atmosphere Dynamics*. Academic Press, Inc.: New York.

Baldwin, M. P., L. Gray, T. Dunkerton, K. Hamilton, P. Haynes, W. Randel, J. Holton, M. Alexander, I. Hirota, T. Horinouchi, D. Jones, J. Kinnersley, C. Marquardt, K. Sato, and M. Takahasi 2001. The Quasi-Biennial Oscillation. *Reviews of Geophysics* **39**, 179-229.

Baines, K., R. W. Carlson and L. W. Kamp 2002. Fresh Ammonia Ice Clouds in Jupiter I. Spectroscopic Identification, Spatial Distribution and Dynamical Implications. *Icarus* **159**, 74-94.

Beebe, R. F., R. M. Suggs and T. Little 1986. Seasonal North-South Asymmetry in Solar Radiation Incident on Jupiter's Atmosphere. *Icarus* **66**, 359-365.

Besanger, C., B. Bézard, and D. Gautier 1986. Spatial variation of the thermal structure of Jupiter's atmosphere. In *The Jovian Atmospheres*, NASA Conf. Publ. 2441, M. Allison and L. D. Travis, eds., pp. 79-81.

Birnbaum, G., A. Borysow, and G. S. Orton 1996. Collision-induced absorption of H_2-H_2 and H_2-He in the rotational and fundamental bands for planetary applications. *Icarus* **123**, 4-22.

Borysow, A., L. Trafton, L. Frommhold, and G. Birnbaum 1985. Modelling of pressure-induced far infrared absorption spectra: Molecular hydrogen pairs. *Astrophys. J.* **296**, 644-654.

Conrath, B. J. and D. Gautier 1980. Thermal structure of Jupiter's atmosphere obtained by inversion of Voyager 1 infrared measurements. In *Interpretation of Remotely Sensed Data*, A. Deepak, ed. Academic Press, New York.

Conrath, B. J., F. M. Flasar, J. Pirraglia, P. Gierasch and G. Hunt 1981. Thermal Structure and Dynamics of the Jovian Atmosphere 2. Visible Cloud Features. *J. Geophys. Res.* **86**, 86- 8769-8775.

Conrath, B. J. and P. J. Gierasch 1984. Global Variation of the para Hydrogen Fraction in Jupiter's Atmosphere and Implications for Dynamics on the Outer Planets. *Icarus* **57**, 184-204.

Conrath, B. J. and P. J. Gierasch 1986. Retrieval of Ammonia Abundances and Cloud Opacities on Jupiter from Voyager IRIS Spectra. *Icarus* **67**, 444-455.

Conrath, B. P. Gierasch and S. Leroy 1990. Temperature and circulation in the stratosphere of the outer planets. *Icarus* **83**, 255-281.

Conrath, B. J., P. J. Gierasch, and E. A. Ustinov 1998. Thermal structure and para hydrogen fraction on the outer planets from Voyager IRIS measurements. *Icarus* **135**, 501-517.

Dunkerton, T. 1978. On the Mean Meridional Mass Motions of the Stratosphere and Mesosphere. *J. Atmos. Sci.* **35**, 2325-2332.

Flasar, F. M., *et al.* 2004a. An intense stratospheric jet on Jupiter. *Nature* **427**, 132-135.

Flasar, F. M., *et al.* 2004b. Exploring the Saturn system in the thermal infrared: the Composite Infrared Spectrometer. *Space Sci. Rev.*, submitted.

Friedson, A. J. 1999. New Observations and Modelling of a QBO-Like Oscillation in Jupiter's Stratosphere. *Icarus* **137**, 34–55

Gierasch, P. J., B. J. Conrath and J. A. Magalhaes 1986. Zonal Mean Properties of Jupiter's Upper Troposphere from Voyager Infrared Observations. *Icarus* **67**, 456-483.

Gierasch, P., A. Ingersoll, D. Banfield, S. Ewald, P. Helfenstein, A. Simon-Miller, A. Vasavada, H. Breneman, D. Senske and the Galileo Imaging Team 2000. Observation of moist convection in Jupiter's atmosphere. *Nature* **403**, 628-629.

Greathouse, T., J. Moses, B. Bézard, C. Griffith, J. Lacy, and M. Richter 2003. Latitudinal variations of temperature, C_2H_2 and C_2H_6 in Saturn's stratosphere with the detection of propane. *Bull. Amer. Astron. Soc.* **35**, 1019.

Hanel, R., B. Conrath, V. Kunde, P. Lowman, W. Maguire, J. Pearl, J. Pirraglia, D. Gautier, P. Gierasch and S. Kumar. 1977. The Voyager infrared spectroscopy and radiometry investigation. *Space Sci. Rev.* **21**, 129-157.

Hanel, R., L. Herath, V. Kunde and J. Pearl 1980a. Voyager Infrared Interferometer Spectrometer and Radiometer (IRIS) – Documentation for Reduced Data Records (RDR) for Jupiter. NASA GSFC Document: X-693-821-8.

Hanel, R., D. Crosby, L. Herath, D. Vanous, D. Collins, H. Creswick, C. Harris and M. Rhodes 1980b. Infrared spectrometer for Voyager. *Applied Optics* **19**, 1391-1400.

Irwin, P., P. Parrish, T. Fouchet, S. Calcutt, F. Taylor, A. Simon-Miller, C. Nixon and F. M. Flasar 2003. Retrievals of Jovian tropospheric phosphine from Cassini CIRS. *Icarus*, submitted.

Kunde, V. G. and 50 Co-authors 1996. Cassini infrared Fourier spectroscopic investigation. *Proc. SPIE* **2803**, 162-177.

Lacy, J. H., M. J. richter, T. K. Greathouse, D. T. Jaffe, and Q. Zhu 2002. TEXES: A sensitive high-resolution grating spectrograph for the mid-infrared. *Pub. Astron. Soc. Pacific* **114**, 153-168.

Leovy, C. B., A. J. Friedson and G. S. Orton 1991. The quasiquadrennial oscillation of Jupiter's equatorial stratosphere. *Nature* **354**, 380-382.

Li, X. and P. L. Read 2000. A mechanistic model of the quasi-quadrennial oscillation in Jupiter's stratosphere. *Planetary and Space Sci.* **48**, 637-669.

Niemann, H., S. Atreya, G. Carignan, T. Donahue, J. Haberman, D. Harpold, R.E. Hartel, D. Hunten, W. Kasprzak, P. Mahaffy, T. Owen, and S. Way 1998. The composition of the jovian atmosphere as determined by the Galileo probe mass spectrometer. *J. Geophys. Res.* **103**, 22,831-22,846.

Orton, G., A. Friedson, J. Caldwell, H. Hammel, K. Baines, J. Bergstrahl, T. Martin, M. Malcolm, R. West, W. Golisch, D. Griep, C. Kaminski, A. Tokunaga, R. Baron and M. Shure 1991. Thermal maps of Jupiter: Spatial organization and time dependence of stratospheric temperatures, 1980–1991. *Science* **252,** 537–542.

Orton, G., A. Friedson, P. Yanamandra-Fisher, J. Caldwell, H. Hammel, K. Baines, J. Bergstrahl, T. Martin, R. West, G. Veeder Jr, D. Lynch, R. Russell, M. Malcolm, W. Golisch, D. Griep, C. Kaminski, A. Tokunaga, T. Herbst and M. Shure 1994. Spatial

organization and time dependence of Jupiter's tropospheric temperatures, 1980–1993. *Science* **265,** 625–631.

Porco, C, R. West, A. McEwen, A. Del Genio, A. Ingersoll, P. Thomas, S. Squyres, L. Dones, C. Murray, T. Johnson, J. Burns, A. Brahic, G. Neukum, J. Veverka, J. Barbara, T. Denk, M. Evans, J. Ferrier, P. Geissler, P. Helfenstein, T. Roatsch, H. Throop, M. Tiscareno, A. Vasavada 2003. Cassini Imaging of Jupiter's Atmosphere, Satellites, and Rings. *Science* **299**, 1541-1547.

Press, W. H., S. A. Teukolsky, W. T. Vetterling and B. P. Flannery 1992. *Numerical recipes in FORTRAN: The art of scientific computing*. Cambridge University Press: New York.

Salby, M. L. 1996. *Fundamentals of Atmospheric Physics*. Academic Press, Inc: New York.

Simon, A. 1999. The Structure and Temporal Stability of Jupiter's Zonal Winds: A Study of the North Tropical Region. *Icarus* **141**, 29-39.

Simon-Miller, A. A., P. Gierasch, R. Beebe, B. Conrath, F. M. Flasar, R. Achterberg and the Cassini CIRS Team 2002. New Observational Results Concerning Jupiter's Great Red Spot. *Icarus* **158**, 249-266.

Vincent, M., J. Clarke, G. Ballester, W. Harris, C. Burrows, J. Gallagher III, R. Griffiths, J. Hester, J. Hoessel, J. Holtzman, J. Mould, P. Scowen, A. Watson and J. Westphal 2000. Jupiter's Polar Regions in the Ultraviolet as Imaged by HST/WFPC2: Auroral-Aligned Features and Zonal Motions. *Icarus* **143**, 205-222.

Von Zahn, U., D.M. Hunten, and G. Lehmacher 1998. Helium in Jupiter's atmosphere: Results from the Galileo probe helium interferometer experiment. *J. Geophys. Res.* **103**, 22,815-22,829.

West, R. A., A. J. Friedson and J. F. Appleby 1992. Jovian Large-Scale Stratospheric Circulation. *Icarus* **100**, 245-259.

Figure Captions

Figure 1. Normalized inversion kernels from selected wavelength regions. The contribution functions from 1313, 1304, 600 and 300 cm^{-1} are displayed as a function of pressure in Jupiter's atmosphere, showing the approximate coverage obtained in the temperature retrievals.

Figure 2. Retrieved temperature maps from Voyager IRIS (top) and Cassini CIRS (bottom). Using multiple spectral regimes, temperatures were retrieved and plotted from roughly 1 to 500 mbar of pressure over latitudes from 55° N to 55° S. The full CIRS map and IRIS troposphere are plotted from smoothed 5° latitude bins on a 2.5° latitude grid, while the IRIS stratosphere retrievals are coarser (10° bins). Temperatures for the region between 20 and 100 mbar are interpolated in both data sets.

Figure 3. Retrieved high-latitude temperature maps from Voyager IRIS (top) and Cassini CIRS (bottom) for the northern (left) and southern (right) hemispheres. The tropospheric temperatures below the tropopause (100 mbar) is shown for latitudes between 55 and 75° latitude.

Figure 4. Zonal winds calculated from the temperature maps shown in Fig. 2. Voyager (Simon 1999) and Cassini (Porco *et al.* 2003) zonal wind profiles are used for the cloud top winds.

Figure 5. Latitudinal temperature variations for the troposphere (~250 mbar, left) and stratosphere (~10-20 mbar, right) from 1979-2001. NASA IRTF data (1980-2000) at 7.8 and 17.9 microns were used to fill in coverage between the Voyager (1979) and Cassini (2001) flybys and to show variations with time. Each year's profile is offset by roughly 5 K for clarity and the tick marks are 5 K apart for a given year.

Figure 6. Cross sections of the zonal mean temperatures in Fig. 2, relative to an global mean vertical profile of temperature, obtained by areally averaging temperatures on each isobar.

Figure 7. Comparison of tropospheric (left) and stratospheric (right) thermal winds. The CIRS thermal winds (solid line) are compared with the IRIS thermal winds (dotted) at 250 mbar (left) and 20 mbar (right). Magnitude and latitudinal variations are evident.

Figure 8. Possible quasi-quadrennial oscillations in the troposphere (left) and stratosphere (right). The difference in equatorial temperature from the average of 15° N and S is used to show equatorial variations. Overplotted is a 4-year periodic signal for comparison.

Figure 9. Periodogram analysis of the temperature differences shown in Figure 8 for 250 mbar (top) and 10-20 mbar (bottom). Confidence levels are plotted for comparison.

Figure 10. Time series of hemispheric temperature differences for 50°, 40°, 30°, 20° and 10° latitude at 250 mbar (top) and 10-20 mbar (bottom).

Figure 11. Periodogram analysis of hemispheric temperature differences for 50°, 40°, 30°, 20° and 10° latitude at 250 mbar (top) and 10-20 mbar (bottom). Power is normalized by the variance in the data. Confidence levels of 60%, 70%, 80% and 90% are shown for comparison. The confidence levels are defined as 1 – the false-alarm probability that a sampling of a white noise spectrum having the same variance as the data could produce a peak in the periodogram with the indicated power or higher.

Figure 12. Cross correlation of subsolar latitude with the temperature contrast T(40N) – T(40S) at 250 mbar (upper panel) and 10-20 mbar (lower panel). The temperatures were taken from the time series in Fig. 5. To deal with the unevenly spaced data in time, the data were interpolated onto an evenly spaced grid.

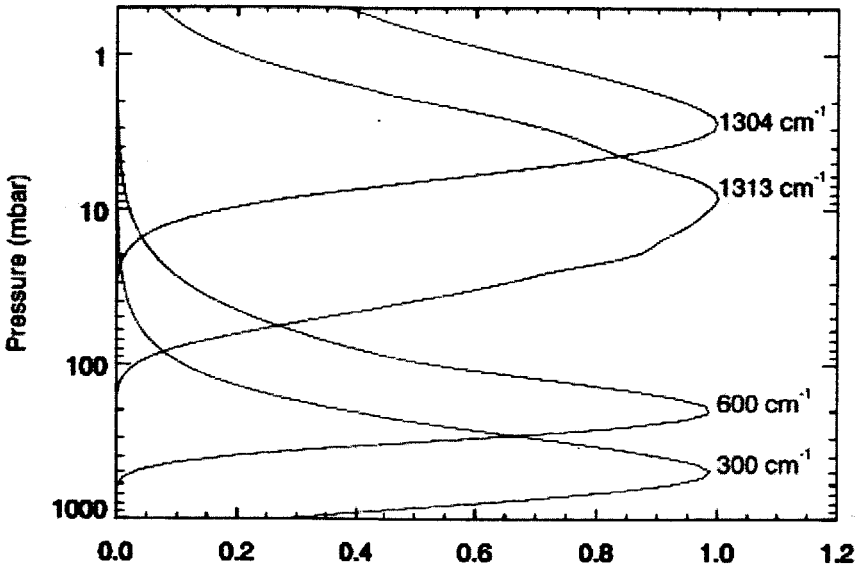
Pressure (mbar)
1
10
100
1000
0.0
0.2
0.4
0.6
0.8
1.0
1.2
1304 cm-1
1313 cm-1
600 cm-1
300 cm-1

Fig 1.

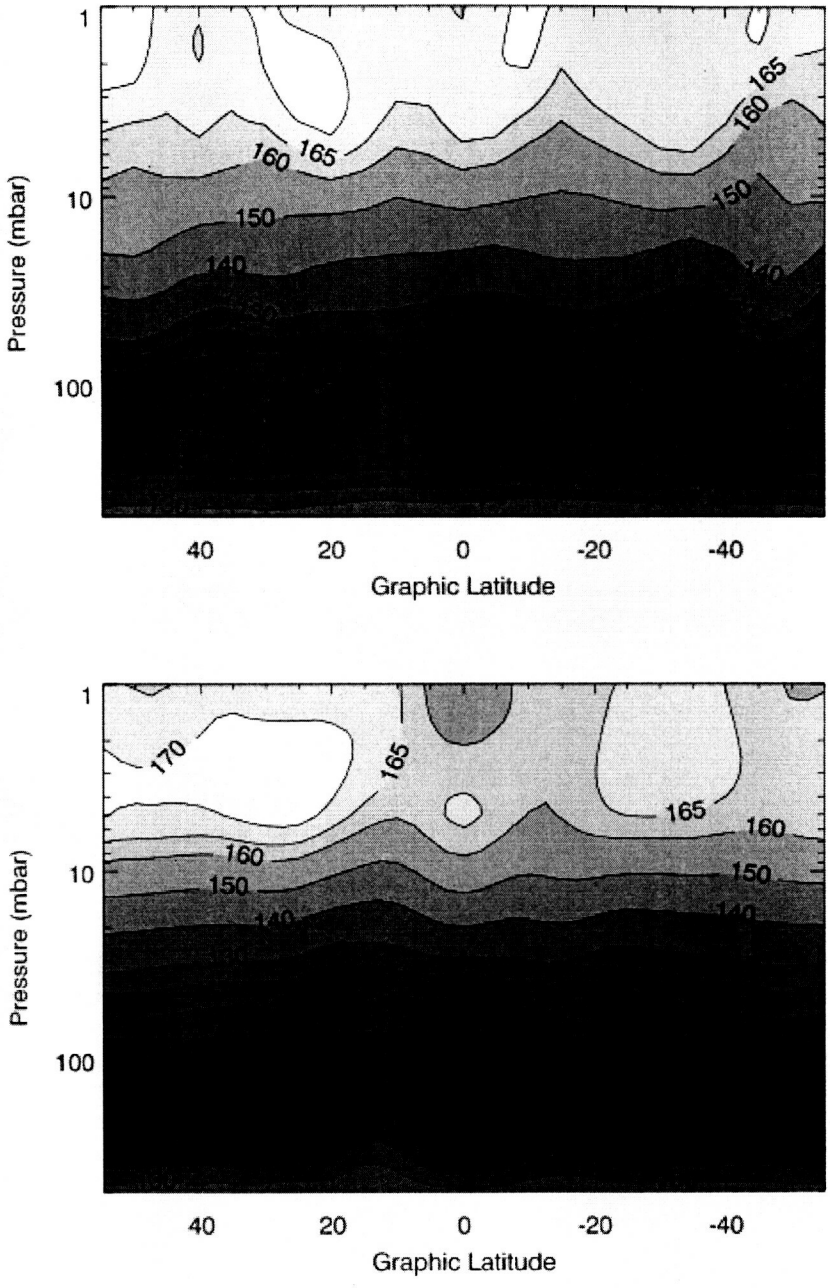
1
10
100
Pressure (mbar)
160
165
150
140
40
20
0
-20
-40
Graphic Latitude
1
10
100
Pressure (mbar)
170
165
160
150
140
40
20
0
-20
-40
Graphic Latitude

Fig. 2.

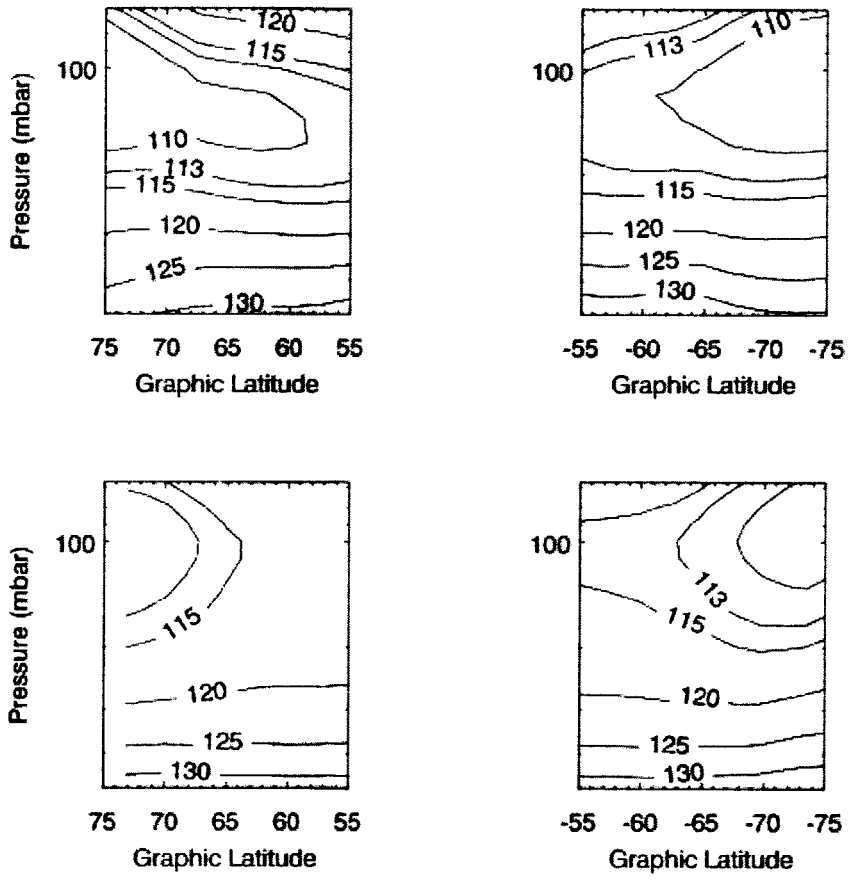
Pressure (mbar)
100
120
115
110
113
115
120
125
130
75 70 65 60 55
Graphic Latitude
100
113
110
115
120
125
130
-55 -60 -65 -70 -75
Graphic Latitude
Pressure (mbar)
100
115
120
125
130
75 70 65 60 55
Graphic Latitude
100
113
115
120
125
130
-55 -60 -65 -70 -75
Graphic Latitude

Fig. 3.

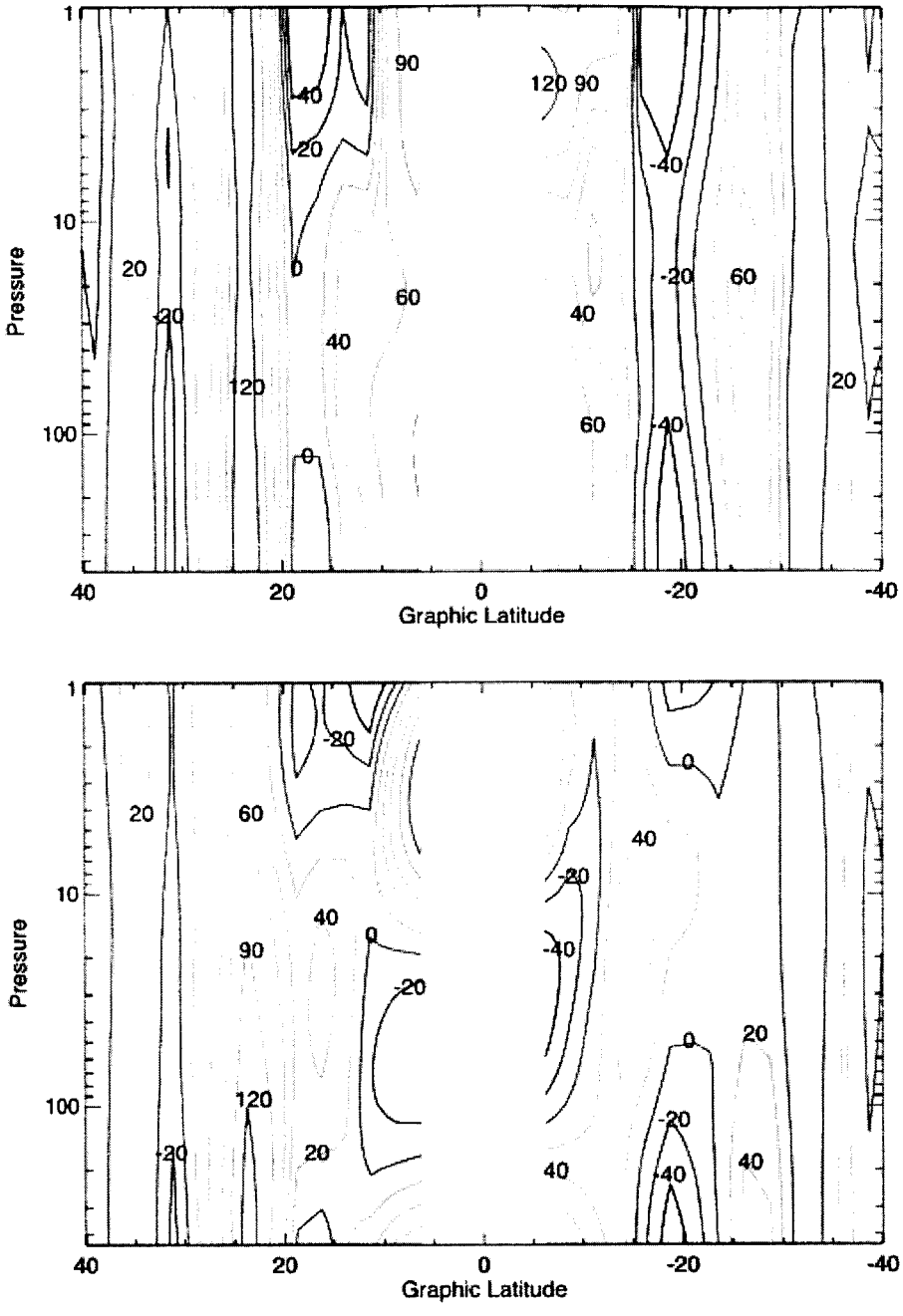
Pressure
1
10
100
90
120 90
-40
-20
20
0
60
40
120
-20
60
20
Graphic Latitude
40
20
0
-20
-40
Pressure
1
10
100
-20
0
20
60
40
90
-40
120
Graphic Latitude
40
20
0
-20
-40

Fig. 4.

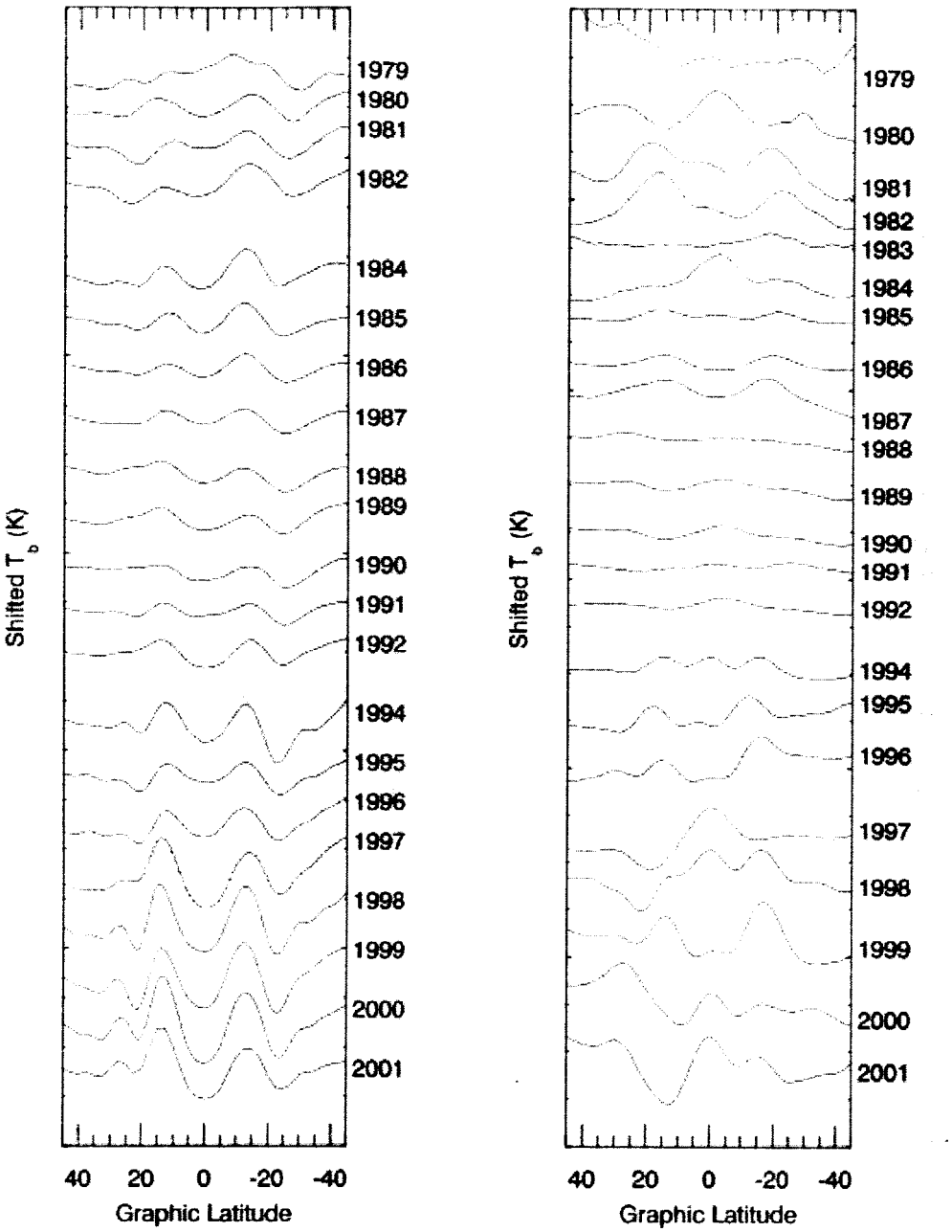
Shifted T_b (K)
1979
1980
1981
1982
1984
1985
1986
1987
1988
1989
1990
1991
1992
1994
1995
1996
1997
1998
1999
2000
2001
40 20 0 -20 -40
Graphic Latitude
Shifted T_b (K)
1979
1980
1981
1982
1983
1984
1985
1986
1987
1988
1989
1990
1991
1992
1994
1995
1996
1997
1998
1999
2000
2001
40 20 0 -20 -40
Graphic Latitude

Fig. 5.

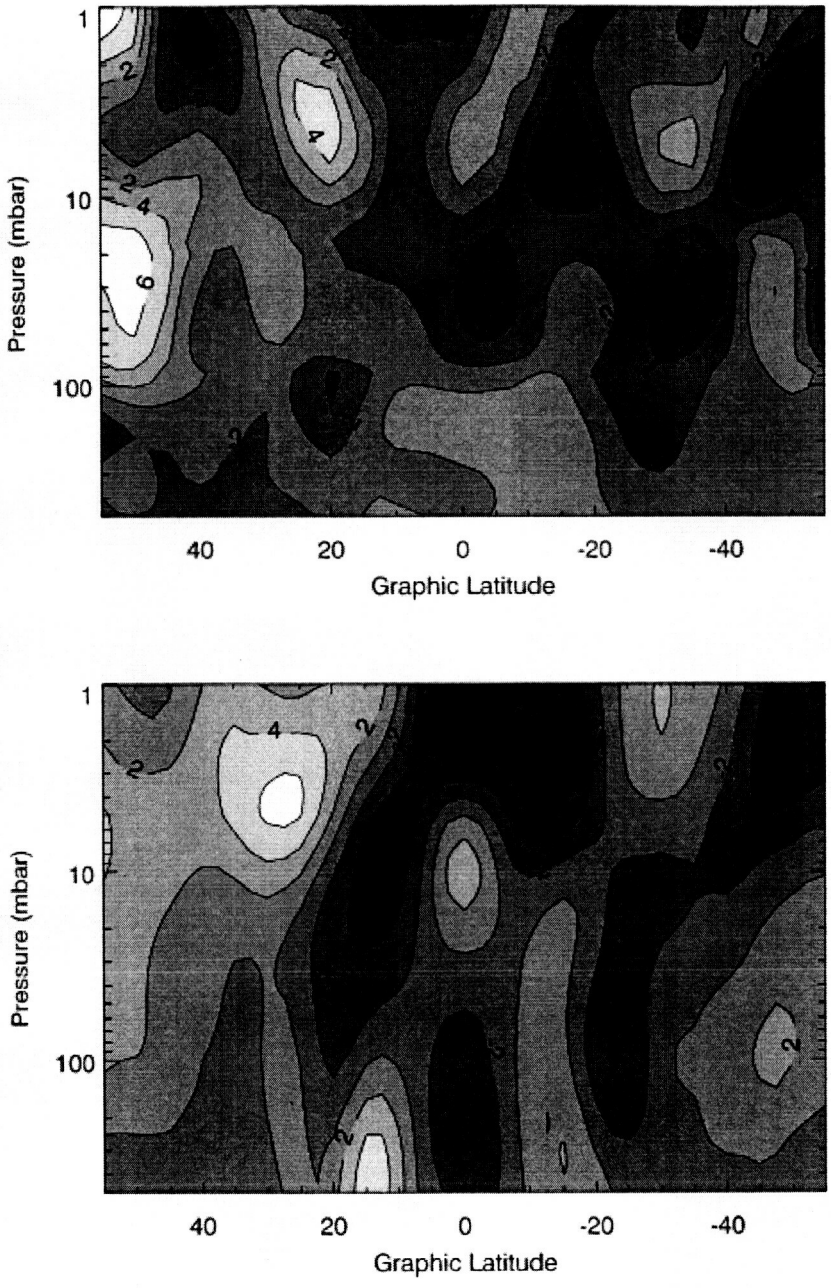
1
10
100
Pressure (mbar)
40
20
0
-20
-40
Graphic Latitude
1
10
100
Pressure (mbar)
40
20
0
-20
-40
Graphic Latitude

Fig 6.

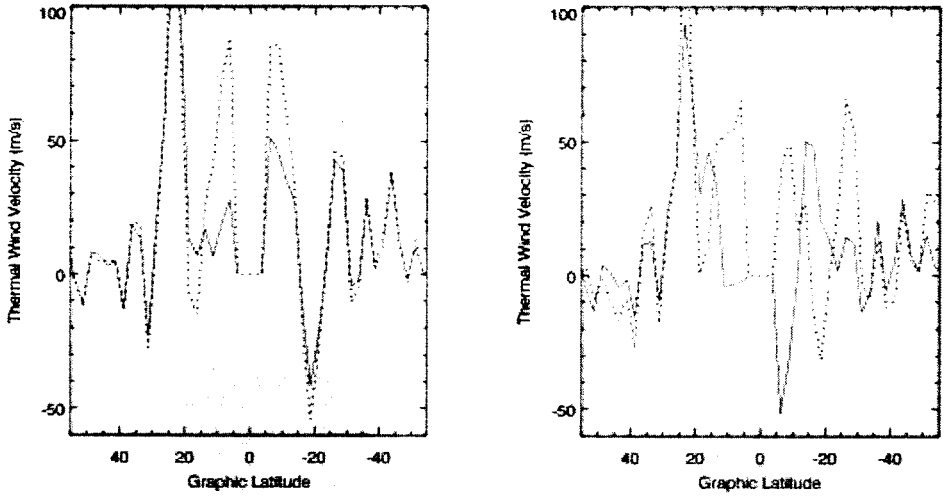
Thermal Wind Velocity (m/s)
100
50
0
-50
40
20
0
-20
-40
Graphic Latitude
Thermal Wind Velocity (m/s)
100
50
0
-50
40
20
0
-20
-40
Graphic Latitude

Fig. 7

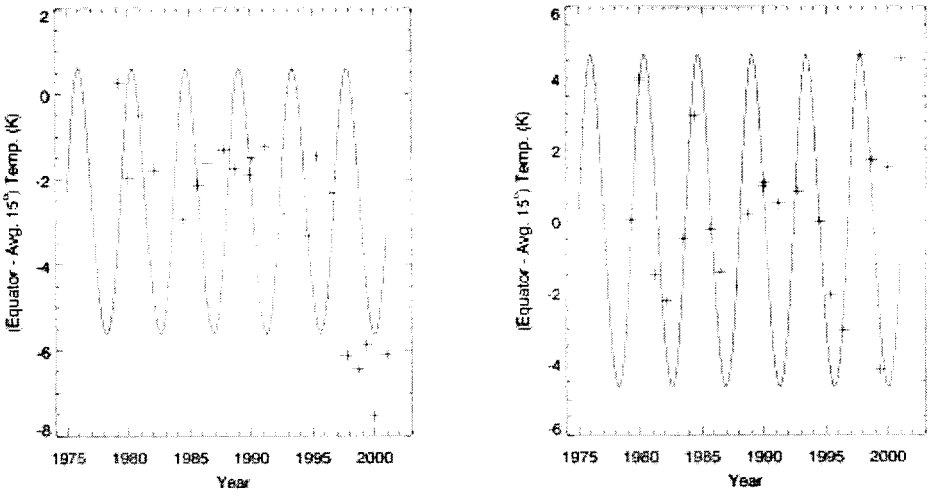
(Equator - Avg. 15°) Temp. (K)
2
0
-2
-4
-6
-8
1975
1980
1985
1990
1995
2000
Year
(Equator - Avg. 15°) Temp. (K)
6
4
2
0
-2
-4
-6
1975
1980
1985
1990
1995
2000
Year

Fig. 8

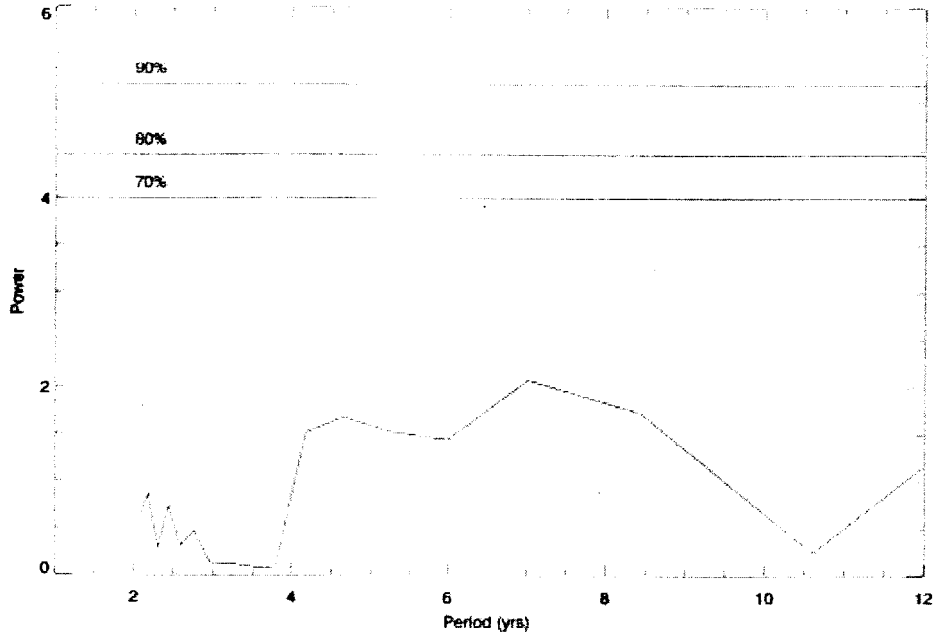

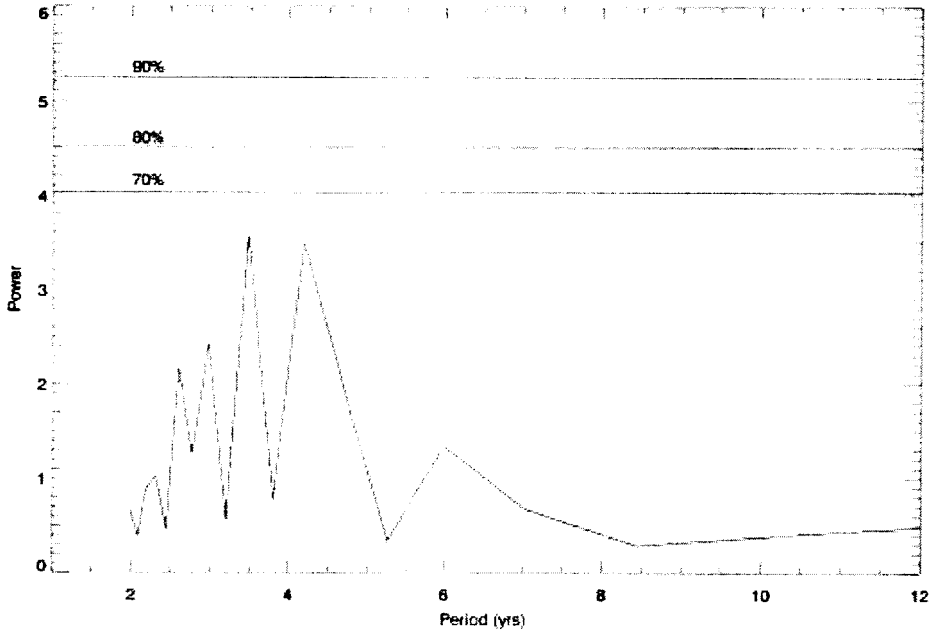

Fig. 9

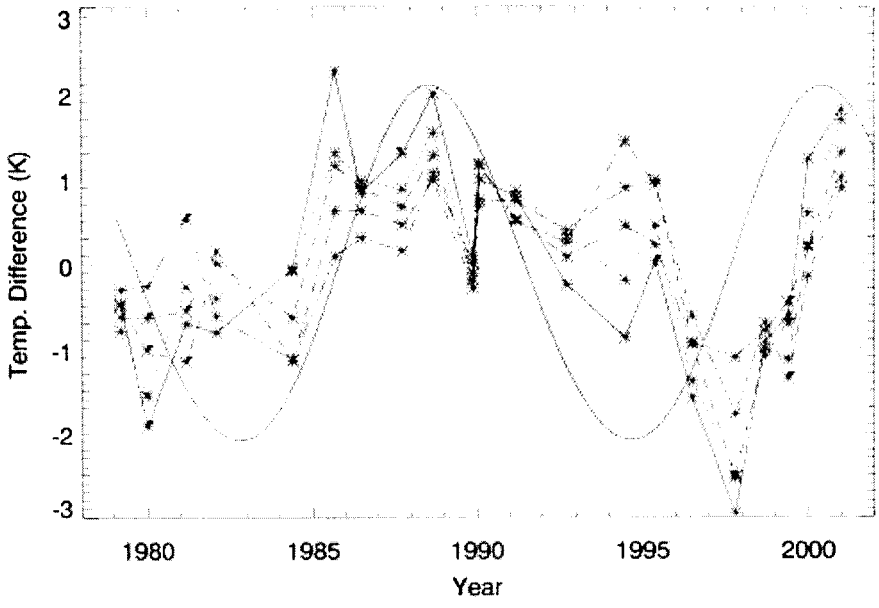
Temp. Difference (K)
3
2
1
0
-1
-2
-3
1980
1985
1990
1995
2000
Year

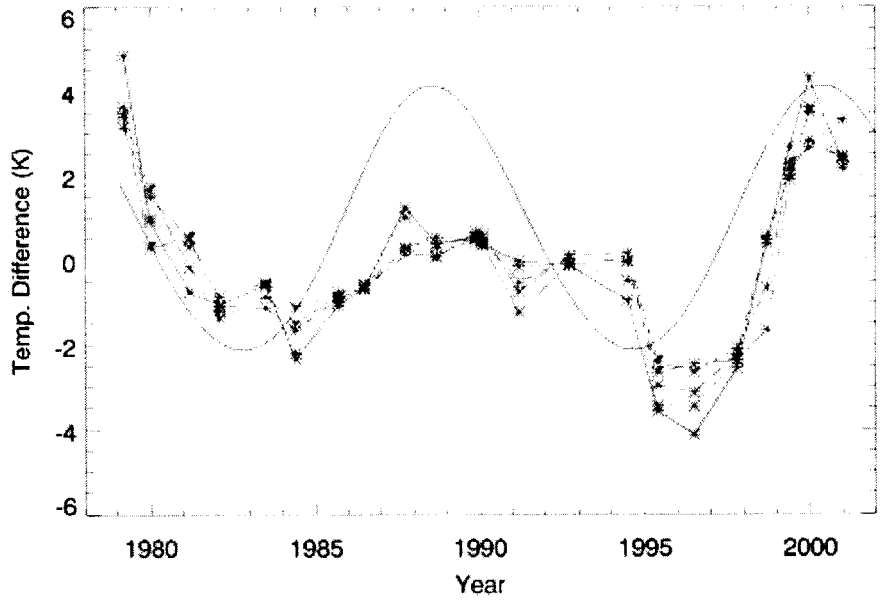
Temp. Difference (K)
6
4
2
0
-2
-4
-6
1980
1985
1990
1995
2000
Year

Fig 10.

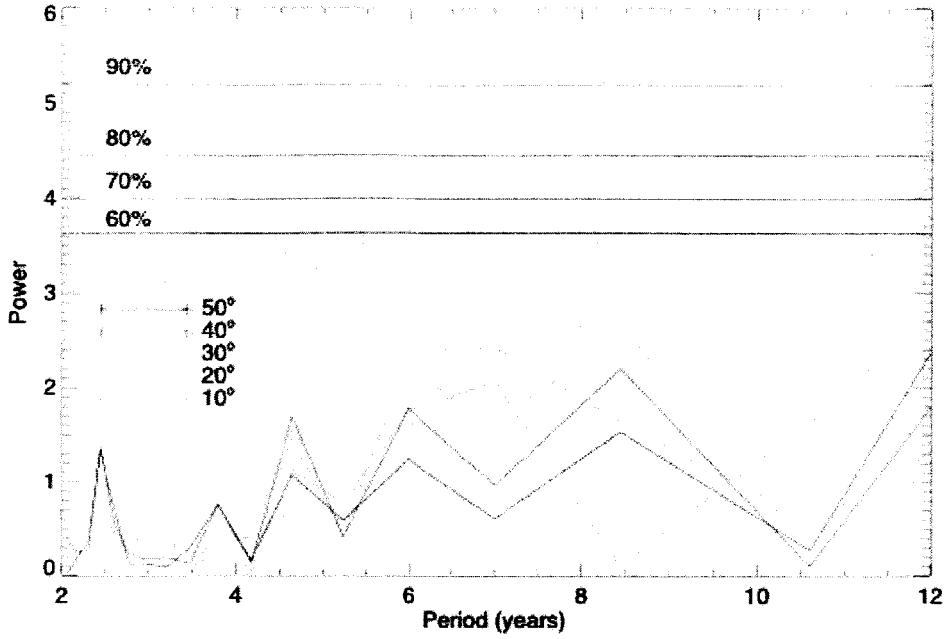
90%
80%
70%
60%
50°
40°
30°
20°
10°
Power
Period (years)

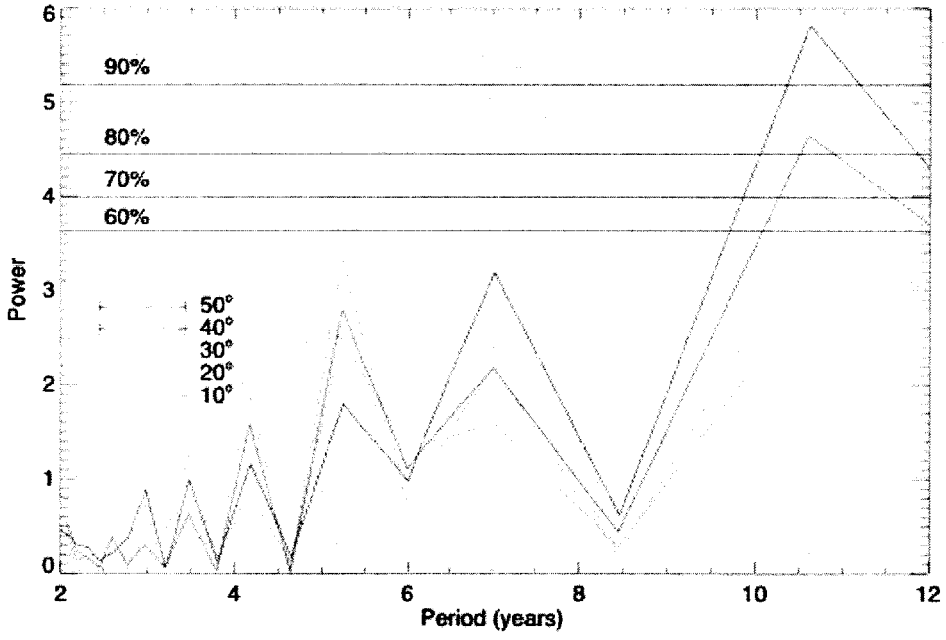
90%
80%
70%
60%
50°
40°
30°
20°
10°
Power
Period (years)

Fig 11

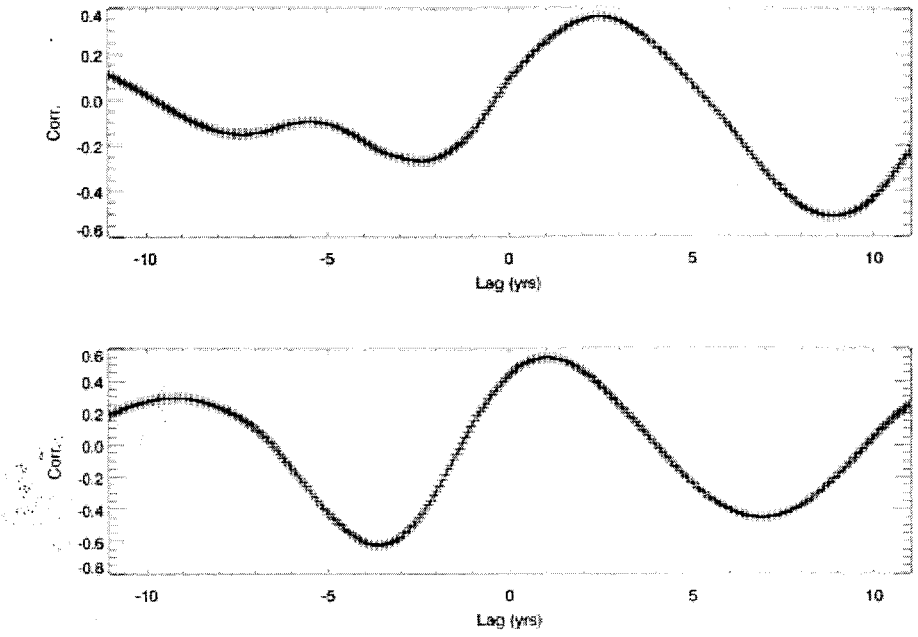
0.4
0.2
0.0
-0.2
-0.4
-0.6
Corr.
-10
-5
0
5
10
Lag (yrs)
0.6
0.4
0.2
0.0
-0.2
-0.4
-0.6
-0.8
Corr.
-10
-5
0
5
10
Lag (yrs)

Fig 12.